

Reconstruction of Abel-transformable images: The Gaussian basis-set expansion Abel transform method

Vladimir Dribinski

Department of Chemistry, University of Southern California, Los Angeles, California 90089-0482

Alexei Ossadtchi

Signal and Image Processing Institute, Department of Electrical Engineering, University of Southern California, Los Angeles, California 90089

Vladimir A. Mandelshtam

Department of Chemistry, University of California at Irvine, Irvine, California 92697

Hanna Reisler^{a)}

Department of Chemistry, University of Southern California, Los Angeles, California 90089-0482

(Received 5 February 2002; accepted for publication 21 March 2002)

In this article we present a new method for reconstructing three-dimensional (3D) images with cylindrical symmetry from their two-dimensional projections. The method is based on expanding the projection in a basis set of functions that are analytical projections of known well-behaved functions. The original 3D image can then be reconstructed as a linear combination of these well-behaved functions, which have a Gaussian-like shape, with the same expansion coefficients as the projection. In the process of finding the expansion coefficients, regularization is used to achieve a more reliable reconstruction of noisy projections. The method is efficient and computationally cheap and is particularly well suited for transforming projections obtained in photoion and photoelectron imaging experiments. It can be used for any image with cylindrical symmetry, requires minimal user's input, and provides a reliable reconstruction in certain cases when the commonly used Fourier–Hankel Abel transform method fails. © 2002 American Institute of Physics. [DOI: 10.1063/1.1482156]

I. INTRODUCTION

The expanding use of photoion and photoelectron imaging in studies of molecular dynamics has brought into focus the need for efficient, high-fidelity image reconstruction.¹ This need has increased recently owing to the improved resolution achieved via velocity map imaging and event-counting and centroiding techniques.^{2–4} Ideally, the image reconstruction method should be able to reproduce the sharpest features in the image, have a large dynamic range, and handle noise well. In order to be used in routine laboratory applications, it is desirable that such a method be fast and general, requiring minimal input from the experimenter.

Fortunately, in many applications of imaging, cylindrical symmetry exists with respect to the polarization vector of the excitation laser. This is the case when the kinetic energy of the charged particles obtained in the acceleration stage is much greater than their photoejection energy. In such cases, the three-dimensional (3D) image, $I=I(r,z)$, is a function of only two coordinates in a cylindrical coordinate system. Let $P(x,z)$ define the 2D projection of $I(r,z)$ on the detector plane, (x,z) , where the x axis is perpendicular to the z axis. The two functions are then related by the Abel integral,⁵

$$P(x,z) = 2 \int_{|x|}^{\infty} \frac{rI(r,z)}{\sqrt{r^2-x^2}} dr. \quad (1)$$

In imaging experiments, the projection $P(x,z)$ is measured as a 2D array $\mathbf{P} \in \mathbf{R}^{N_x \times N_z}$ with elements defined on an evenly spaced 2D grid $(x_i, z_j) = (i\Delta, j\Delta)$ of sensors (or pixels) with the total number $N_x \times N_z$ usually ranging from 10^5 to 10^6 . In this case

$$\mathbf{P}_{ij} = 2 \int h(x-x_i, z-z_j) dx dz \int_{|x|}^{\infty} \frac{rI(r,z)}{\sqrt{r^2-x^2}} dr, \quad (2)$$

where $h(x,z)$ defines an instrumental function to be specified later.

The quantity of interest is the image $I(r,z)$, which can in principle be obtained directly by evaluating the inverse Abel transform,⁶

$$I(r,z) = -\frac{1}{\pi} \int_r^{\infty} \frac{[dP(x,z)/dx]}{\sqrt{x^2-r^2}} dx. \quad (3)$$

However, using Eq. (3) is numerically impractical as it has singularities and requires derivative estimation for a generally noisy function defined on a grid. Although attempts to use Eq. (3) were made (e.g., by fitting the experimental data at each slice $z = \text{const}$ with analytical functions, and using Eq. (3) to find the inverse Abel transform with analytically computed derivatives),^{7–9} none of the proposed methods was successful in achieving high quality inversion, especially for noisy projections.

Currently, the most commonly used method for calculating the inverse Abel transform in charged particle imaging

^{a)}Electronic mail: reisler@usc.edu

applications is the Fourier–Hankel technique.¹⁰ This method is based on a representation of the inverse Abel transform (3) via the Hankel transform of the Fourier transform of the projection.¹⁰ It is widely used for reconstruction of imaging data, as it is fast and produces satisfactory results for high-quality images with a small dynamic range. However, the method magnifies experimental noise and also produces artificial structures when reconstructing images with high-intensity sharp features. These artificial structures are dependent on the particular fast Fourier transform and discrete Hankel transform algorithms used and, thus, differ for different implementations of the Fourier–Hankel method. Furthermore, as demonstrated in Sec. III, the artificial structures extend through the entire reconstructed image, causing a reduction in resolution and in signal-to-noise ratio. In fact, the Fourier–Hankel method becomes practically unusable in cases of excessively noisy images, or images with a large dynamic range.

Recently, several methods have been developed in order to alleviate these problems and achieve reliable transformation of noisy experimental projections.¹ Although they work better than the Fourier–Hankel transform in many cases, they also have drawbacks. The back-projection method introduced by Matsumi and co-workers employs filtering in the frequency domain to reduce experimental noise.¹¹ This is done at a cost of smoothing the data and, therefore, a potential loss of information. The back-projection procedure developed by Helm and co-workers is too complicated and time-consuming to be used in routine applications and requires specific input parameters for each system.^{12,13} The simplified “onion peeling” method does not handle well noisy images; e.g., the noise in the reconstructed image increases progressively towards the center.^{12,13} The iterative procedure of Vrakking does not have reconstruction artifacts, but is slow.¹⁴

In this article we describe a new image reconstruction method that can serve as an alternative to the Fourier–Hankel transform method, but does not have its limitations. The method is efficient and computationally cheap and is particularly well suited for transforming projections obtained in photoion and photoelectron imaging experiments. It can be used for any image with cylindrical symmetry, requires minimal user’s input, and provides a reliable reconstruction in certain cases when the Fourier–Hankel transform method fails.

The method is based on representing the *image* as an expansion in a well-behaved basis set in the image r, z space, and using Eq. (2) to generate the basis in the projection space. The latter will be smooth because the forward Abel integral (2), in contrast to the expression for the inverse Abel transform (3), is a well-behaved operation. In order to avoid any numerical instability, it is desirable to evaluate the transforms analytically, which implies certain restrictions on the choice of the basis. We call this method the basis set expansion (BASEX) Abel transform method for image reconstruction. We show how by using a suitable basis set, we convert the ill-posed inverse problem into a simple problem of finding expansion coefficients, a procedure that requires only matrix multiplication. We also demonstrate that the new

method works well in situations that cannot be handled by the regular Fourier–Hankel method.

The article is organized as follows. Section II gives a general description of the method along with a description of the specific basis set used in our work. Section III demonstrates the performance of the new method and compares it with the Fourier–Hankel method, for which two different codes were used: the first was developed by Strickland and Chandler,¹⁵ and the second is based on the algorithm given by Whitaker in Ref. 1. We end by discussing in Sec. IV the advantages of the BASEX method and some possible modifications and extensions.

II. DESCRIPTION OF THE METHOD

A. BASEX: The basis set expansion method for an ill-posed inverse problem

Consider a set of 2D functions in the image space $\{f_k(r, z)\}$ ($k=0, \dots, K-1$) to be specified later, and the corresponding transformed set of vectors $\{\mathbf{G}_k \in \mathbf{R}^{N_x \times N_z}\}$ ($k=0, \dots, K-1$) defined in the projection space. The two sets are assumed to be related via Eq. (2):

$$\mathbf{G}_{kij} = 2 \int h(x-x_i, z-z_j) dx dz \int_{|x|}^{\infty} \frac{rf_k(r, z)}{\sqrt{r^2-x^2}} dr. \quad (4)$$

We further assume that both sets are well-behaved and, in particular, form good bases, so we can use the expansions:

$$I(r, z) = \sum_{k=0}^{K-1} \mathbf{C}_k f_k(r, z), \quad (5)$$

$$\mathbf{P}_{ij} = \sum_{k=0}^{K-1} \mathbf{C}_k \mathbf{G}_{kij}. \quad (6)$$

In the matrix form

$$\mathbf{P} = \mathbf{C}\mathbf{G}, \quad (7)$$

with the coefficients vector $\mathbf{C} = (\mathbf{C}_0, \dots, \mathbf{C}_{K-1})$ and the basis transformation matrix $\mathbf{G} = (\mathbf{G}_0, \dots, \mathbf{G}_{K-1})^T$. Note that in general, the total number, K , of basis functions may be greater or smaller than the total number, $N_x \times N_z$, of pixels, which then results in, respectively, an under- or overdetermined problem. In such cases the inverse \mathbf{G}^{-1} does not exist. A solution of the corresponding least-squares problem can be obtained by Tikhonov regularization:¹⁶

$$\mathbf{C} = \mathbf{P}\mathbf{G}^T(\mathbf{G}\mathbf{G}^T + q^2\mathbf{I})^{-1}, \quad (8)$$

where \mathbf{I} is the identity matrix and q is a regularization parameter. The regularization is used to improve the condition number of the matrix $\mathbf{G}\mathbf{G}^T$ (i.e., the ratio of the highest and lowest singular values), which may be ill-conditioned (have a large condition number), or even singular (if $K > N_x \times N_z$).

In principle, it would be most desirable to implement a nonseparable 2D basis of size K , which would require inversion of the $K \times K$ matrix $\mathbf{G}\mathbf{G}^T + q^2\mathbf{I}$. Unfortunately, in the present case K is too large (order of 10^5 to 10^6) to be handled numerically, unless a special basis optimized for particular images is used. However, the numerical burden can be alle-

viated considerably by utilizing the separability of the present problem, which allows the use of a direct-product basis set of size $K_x \times K_z$:

$$I(r, z) = \sum_{k=0}^{K_x-1} \sum_{m=0}^{K_z-1} C_{km} \rho_k(r) \zeta_m(z), \quad (9)$$

$$P_{ij} = \sum_{k=0}^{K_x-1} \sum_{m=0}^{K_z-1} C_{km} X_{ki} Z_{mj}. \quad (10)$$

In the matrix form

$$P = X^T C Z, \quad (11)$$

with

$$X_{ki} = 2 \int h_x(x - x_i) dx \int_{|x|}^{\infty} \frac{r \rho_k(r)}{\sqrt{r^2 - x^2}} dr, \quad (12)$$

$$Z_{mj} = \int h_z(z - z_j) \zeta_m(z) dz.$$

A solution of Eq. (11) is given by

$$C = A P B, \quad (13)$$

with $A = (X X^T + q_1^2 I)^{-1} X$ and $B = Z^T (Z Z^T + q_2^2 I)^{-1}$. Because the matrices A and B do not depend on the data matrix P , they could be computed once and then restored from a disk whenever needed. The overall numerical cost of the image reconstruction is, therefore, defined only by a few matrix multiplications.

Clearly, the two transformations in Eq. (13) are completely independent. The way the transformation along the z axis is implemented is not of crucial importance as its only purpose is to smooth the image and incorporate certain constraints, such as symmetry, $I(r, z) = I(r, -z)$.

B. The choice of basis set

Any basis $\rho_k(r)$ would suffice as long as it can be analytically integrated [cf. Eq. (12)] and is uniform, i.e., can account for sharp features of the size of one pixel and is smooth on a smaller scale. Our choice, which satisfies these criteria, is

$$\rho_k(r) = (e/k^2)^{k^2} (r/\sigma)^{2k^2} e^{-(r/\sigma)^2} (k=0, \dots, K_x-1), \quad (14)$$

where the parameter σ is of the order of Δ , the distance between the pixels. Furthermore, we set $K_x \leq (N_x + 1)/2$ so the matrix $X X^T$ is well-conditioned, i.e., it has a small condition number. $\rho_k(r)$ has a maximum at $r = k\sigma$ and is practically indistinguishable from a Gaussian function, i.e., $\rho_k(r) \approx e^{-2(r/\sigma - k)^2}$ for sufficiently large k . A set of such functions constitutes a basis that fills the image space uniformly. The integral over r in Eq. (12) can be evaluated analytically, leading to

$$X_{ki} = \int h_x(x - x_i) \chi_k(x) dx,$$

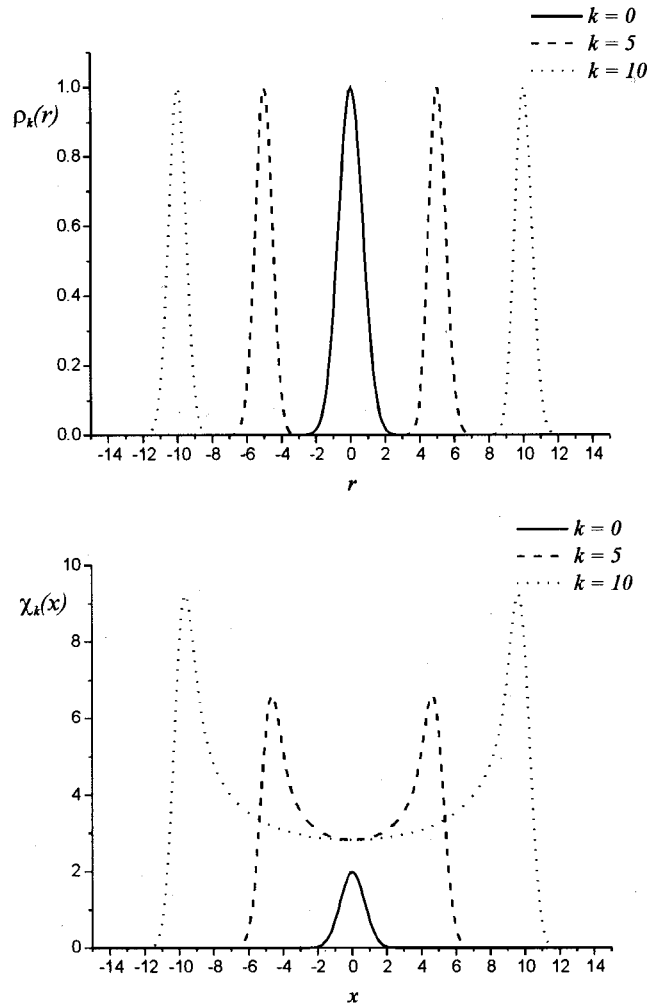


FIG. 1. Examples of basis functions $\rho_k(r)$ (top panel) and the corresponding projections $\chi_k(x)$ (bottom panel) for $k=0, 5,$ and 10 and $\sigma=1$.

$$\chi_k(x) = 2\sigma \rho_k(x) \left[1 + \sum_{l=1}^{k^2} (x/\sigma)^{-2l} \times \prod_{m=1}^l \frac{(k^2 + 1 - m)(m - 1/2)}{m} \right]. \quad (15)$$

Figure 1 shows plots of $\rho_k(r)$ for $k=0, 5,$ and 10 (upper panel) and the corresponding projections $\chi_k(x)$ (lower panel) for $\sigma=1$. (Note that even though $\rho_k(r)$ needs to be defined for $r \geq 0$, we show it in the $[-\infty, +\infty]$ range, as this function is also used to represent the z and x dependencies.) The latter are symmetric functions, $\chi_k(x) = \chi_k(-x)$, which are also highly peaked with maxima at $x \approx \pm k\sigma$. Since $\rho_k(r)$ already includes some broadening, the use of an instrumental function will hardly make a difference in the results. Therefore, for simplicity, we assume $h_x(x) = \delta(x)$, which gives $X_{ki} = \chi_k(x_i)$.

To reduce the number of adjustable parameters, the basis $\zeta_m(z)$ along the z axis is chosen equivalent to that for the r variable, i.e., we use $\zeta_m(z) = \rho_m(z)$ with $Z_{mj} = \rho_m(z_j)$ ($m = 0, \dots, K_z - 1$). Since $\zeta_m(z) = \zeta_m(-z)$, this also incorporates the symmetry constraint. If $K_z \leq (N_z + 1)/2$, the matrix $Z Z^T$ is well-conditioned and has an additional smoothing effect. In our current application with $N_x = N_z = 1001$, we use two

types of basis sets depending on the measured projection: (i) $K_z=K_x=226$, $\sigma=2$, $q_1^2=50$, $q_2^2=0$ and (ii) $K_z=K_x=251$, $\sigma=1$, $q_1^2=5$, $q_2^2=0$. (Note that the value $q_1^2=50$ is very small compared to the average value of the matrix elements of \mathbf{XX}^T .) An efficient algorithm for the numerical evaluation of the functions $\rho_k(r)$ and $\chi_k(x)$ is given in the Appendix.

III. RESULTS

A. Performance of the BASEX Abel-transform method with synthetic images

The performance of the BASEX method with the basis sets described above was first tested in reconstructing a syn-

thetic image from its noise-free projection [calculated by numerical evaluation of the Abel integral (1)], and comparing the results with those obtained with the Fourier–Hankel transform. The model image contains structures most commonly observed in velocity map imaging experiments. Some of these structures, such as high-intensity rings near the center and narrow rings with very sharp edges superimposed on a low-intensity broad feature in the central region, cause problems when reconstructed with the Fourier–Hankel transform. Also note that the narrow rings have different angular distributions, while the broad central feature is isotropic.

The mathematical expression for the model image is

$$I(R, \theta) = 2000(7e^{[(R-10)^2/4]} \sin^2 \theta + 3e^{[(R-15)^2/4]} + 5e^{[(R-20)^2/4]} \cos^2 \theta) + 200(e^{[(R-70)^2/4]} + 2e^{[(R-85)^2/4]} \cos^2 \theta + e^{[(R-100)^2/4]} \sin^2 \theta) + 50(2e^{-[(R-145)^2/4]} \sin^2 \theta + e^{[(R-150)^2/4]} + 3e^{[(R-155)^2/4]} \cos^2 \theta) + 20e^{-[(R-45)^2/3600]}, \quad (16)$$

where R is the distance from the center of the image and θ is the angle between R and the axis of symmetry (vertical axis). These coordinates are related to r , z , such that $r=R \sin \theta$ and $z=R \cos \theta$. Figures 2(a) and 2(b) show a 2D cut of the synthetic image in two different brightness scales to emphasize, respectively, the high- and low-intensity parts of the image.

Figures 3(a) and 3(b) present 2D cuts of the reconstructed images obtained by using the BASEX method and the Fourier–Hankel transform, respectively. Figures 3(c) and 3(d) show the same images with emphasized low-intensity regions. As seen in Figs. 3(b) and 3(d), even in this noise-free case, the Fourier–Hankel transform method produces artificial structures, evident most prominently close to the center of the image. These structures, however, affect not only the central part of the reconstructed image but are spread throughout the entire image area. The BASEX method [Figs. 3(a) and 3(c)] does not generate artificial structures and treats successfully signals of both low and high intensities. We have also used the BASEX method in reconstructing synthetic images with extremely high intensity at the center, a situation for which the regular Fourier–Hankel transform fails completely. Even for this difficult case, the new method produces high quality images.

A different perspective is shown in Fig. 4. The upper panel shows the generated speed distributions

$$P(v) = \frac{1}{P_{\max}} \int_0^\pi I(v, \theta) v^2 \sin \theta d\theta, \quad (17)$$

i.e., the signal integrated over angle at each particular radius R . Here, $(P_{\max})^{-1}$ is the normalization constant, and the particle speed is given by $v=kR$ (k is chosen to be unity for simplicity, so that (v, θ) corresponds to (R, θ) as defined above). Two different approaches were used in deriving the speed distribution. In the first approach it was obtained by using the approximate equation,

$$P(v) \approx \frac{1}{P_{\max}} \sum_{n=0}^v I\left(v, \frac{\pi n}{2v}\right) v \sin\left(\frac{\pi n}{2v}\right), \quad (18)$$

where $v=1, \dots, v_{\max}$, and $I(v, \pi n/2v)$ is calculated as a weighted average of four surrounding points on the image.

Additionally, in the BASEX method, the basis functions could be integrated analytically using Eq. (17), and therefore the speed distribution is given by the exact equation

$$P(v) = \frac{1}{P_{\max}} \sum_{k=0}^{K_x-1} \sum_{m=0}^{K_z-1} v^2 \mathbf{C}_{km} b_{km} R_{m^2+k^2}(v), \quad (19)$$

where \mathbf{C}_{km} are the expansion coefficients, $b_{km} = \{(k^2 + m^2)^{k^2+m^2} / [(k^2)^{k^2} (m^2)^{m^2}]\} \int_{-1}^1 (1-\tau^2)^{k^2} (\tau^2)^{m^2} d\tau$, and $R_n(v) = (e/n)^n v^{2n} e^{-v^2}$. The coefficients b_{km} are evaluated numerically. The two approaches were found to produce similar speed distributions, with the distribution obtained with Eq. (19) having a slightly better resolution.

The lower panel of Fig. 4 shows the differences between the speed distribution computed for the synthetic image and those obtained from the two reconstructed images shown in Fig. 3. The solid line shows the difference with the distribution obtained using the BASEX method, and the dotted line is the corresponding difference for the Fourier–Hankel transform method. The speed distribution obtained for the image reconstructed using the BASEX method essentially coincides with the one obtained directly from the synthetic image. The speed distribution extracted using the Fourier–Hankel method has a poorer resolution due to contributions from the reconstruction artifacts. Since these artifacts have intensities comparable to those of the broad central ring, the latter is hard to identify.

The difference between the two methods is even more pronounced in the angular distributions, which are characterized by the anisotropy parameter β ,¹⁷ given by

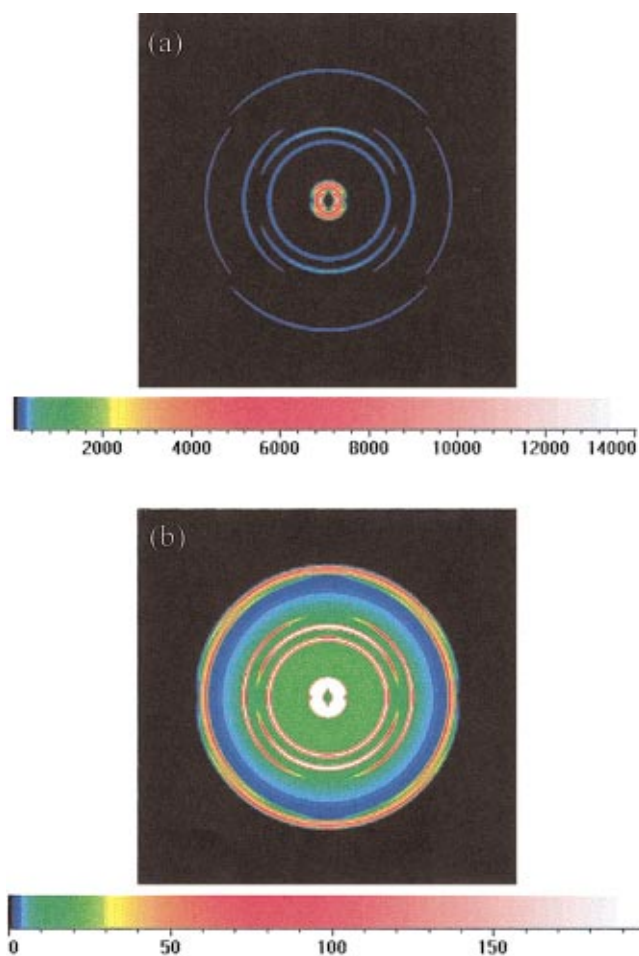


FIG. 2. (Color) (a) A synthetic image plotted in false-color scale (shown with the corresponding numerical scale). (b) Same image plotted on a different color scale that emphasizes the low-intensity parts.

$$P(\theta) \propto \frac{1}{4\pi} [1 + \beta \cdot P_2(\cos \theta)]. \quad (20)$$

As shown in Fig. 5, while the $\beta(v)$ values extracted from the image reconstructed using the BASEX method are identical to those of the synthetic image, the values obtained by using the Fourier–Hankel transform exhibit large deviations, especially in regions where the signal intensity is low. For example, while the broad feature underlying the middle cluster of three sharp peaks has $\beta = 0$, the Fourier–Hankel method gives large negative values.

B. Reconstruction of experimental images

The BASEX method was also applied to the reconstruction of 3D images from experimentally obtained projections that cover a large dynamic range and display different types and levels of noise. As input, we used projections obtained in our own experiments by monitoring photofragment ions, as well as those sent to us by other investigators. We had no problem analyzing any Abel-transformable image that could be inverted by another method, such as those described in Sec. I.

Here we discuss two examples. The first is an image obtained by resonantly enhanced multiphoton ionization de-

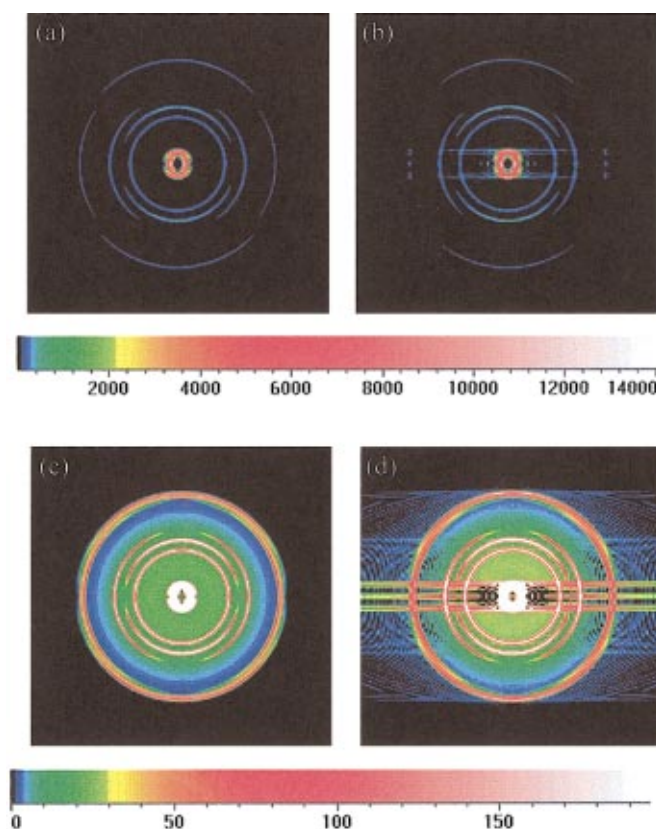


FIG. 3. (Color) (a) 2D cut of the image reconstructed from the projection of the synthetic image shown in Fig. 2 by using the BASEX method and plotted on the same scale as in Fig. 2(a). (b) 2D cut of the image reconstructed using the Fourier–Hankel method (Ref. 15). (c) and (d) show the same images as in (a) and (b), respectively, but plotted on the scale of Fig. 2(b).

tection of $\text{Cl}(^2P_{3/2})$ photofragments obtained in the photodissociation of the CH_2Cl radical at 266 nm.¹⁸ The reconstructed image should exhibit a high-intensity narrow ring with $\beta \cong -1$ located at a large distance from the center, followed by additional, lower-intensity rings at larger radii. These rings correspond to dissociation of ground state and vibrationally excited (“hot band”) CH_2Cl radicals. The experimental image contains, however, additional ion signals not related to the dissociation of CH_2Cl at 266 nm. These signals include: (i) a bright central spot arising from Cl atoms with no translational energy produced by pyrolysis in the radical source along with CH_2Cl ; (ii) a broad distribution of low-speed Cl atoms, which are likely produced by photodissociation of species in the beam other than CH_2Cl ; and (iii) Cl atoms with a very broad speed distribution arising from the photodissociation of CH_2Cl by the probe laser (235.34 nm). In addition to these background signals, the experimental image, which is of low overall intensity, includes non-Abel-transformable statistical noise. In order to observe the signal of interest on top of the large background signals, it is crucial that the reconstruction algorithm remains stable with respect to noise and achieves the highest resolution in separating the contributions from the outer “hot band” rings.

Figures 6(a) and 6(b) show 2D cuts of the images reconstructed from the experimental projection using the BASEX and Fourier–Hankel methods, respectively, and Fig. 7 shows

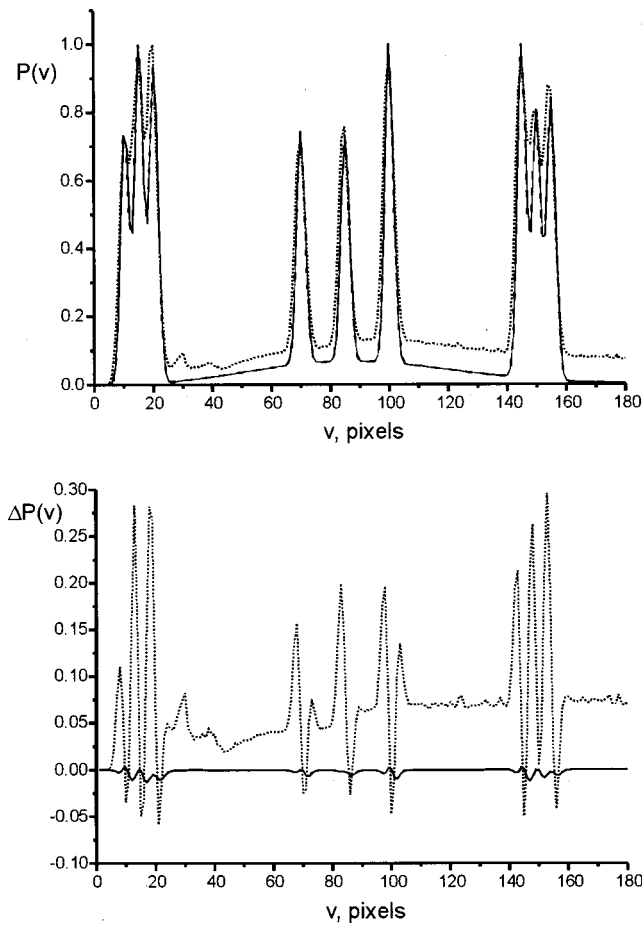


FIG. 4. Top panel: Speed distributions obtained from the synthetic image (solid line), the image reconstructed using the BASEX method (dashed line), and the Fourier–Hankel method (dotted line). Notice that the solid and dashed curves coincide. Bottom panel: The differences between the speed distributions obtained for the image reconstructed using the BASEX method and the synthetic image are shown by the solid line, and the corresponding differences between the Fourier–Hankel method and the synthetic image are shown by the dotted line.

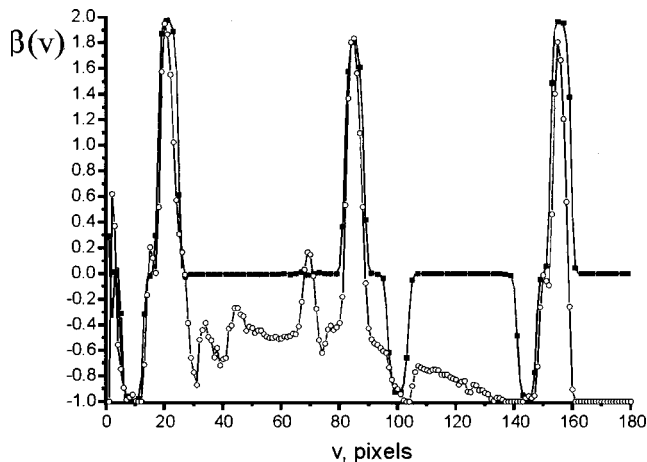


FIG. 5. Anisotropy parameter, $\beta(v)$, distributions for the synthetic image (solid line), image reconstructed using the BASEX method (solid squares; indistinguishable from the synthetic image values), and image reconstructed using the Fourier–Hankel method (open circles connected by line).

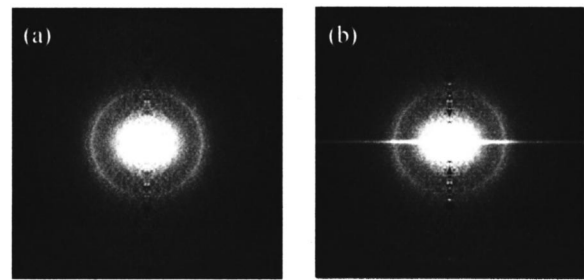


FIG. 6. 2D cuts of images reconstructed from an experimental projection obtained by monitoring $\text{Cl}(^2P_{3/2})$ produced by 266 nm photodissociation of CH_2Cl and detected at 235.34 nm by using (a) the BASEX ($\sigma=1$) and (b) the Fourier–Hankel method (Ref. 15). The intensity scale was chosen to allow observation of the faint outer rings.

the corresponding speed distributions. Evidently, the new method is superior in terms of treating the noise and the achievable resolution (see in particular the region of pixels 80–120).

As a second example, we show an experimental photoion image (projection) obtained by monitoring O^+ ions from the dissociative photoionization of O_2 [Fig. 8(a)].¹⁹ This projection was obtained by using the event-counting technique. In this method, detection of a single electron or ion followed by thresholding (disregarding signals with intensities smaller than a specified threshold value) and centroiding (finding the exact position of the “center of mass” of the spot from each electron or ion) gives increased resolution and eliminates noise produced by the data acquisition system. However, because of the necessity to work at low signal levels, such images possess a high level of statistical noise, i.e., they can have large point-to-point fluctuations in the signal. This is in contrast with multiple-ion detection schemes, which usually produce smooth and continuous images. In order to reconstruct such images, some type of smoothing of the experimental projection is usually needed (e.g., broadening of each spot of the projection by a Gaussian function prior to reconstruction, combining several adjacent pixels, etc.). This smoothing procedure may result in some distortion of the true image. It is noteworthy, therefore, that the BASEX method can handle images with large point-to-point fluctua-

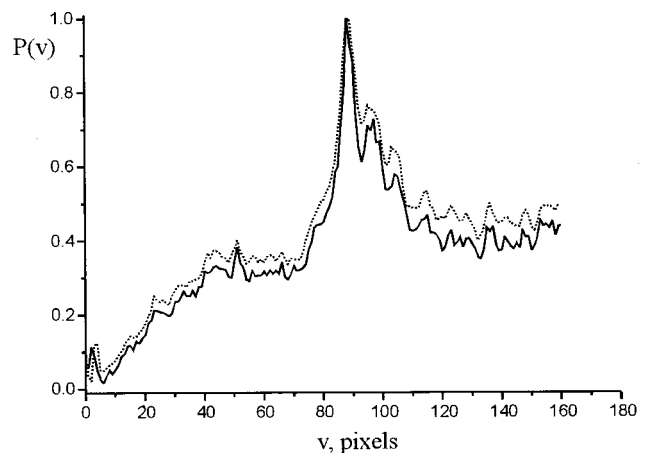


FIG. 7. Speed distributions obtained from the $\text{Cl}(^2P_{3/2})$ images shown in Fig. 6 reconstructed using the BASEX (solid line) and Fourier–Hankel (dotted line) methods.

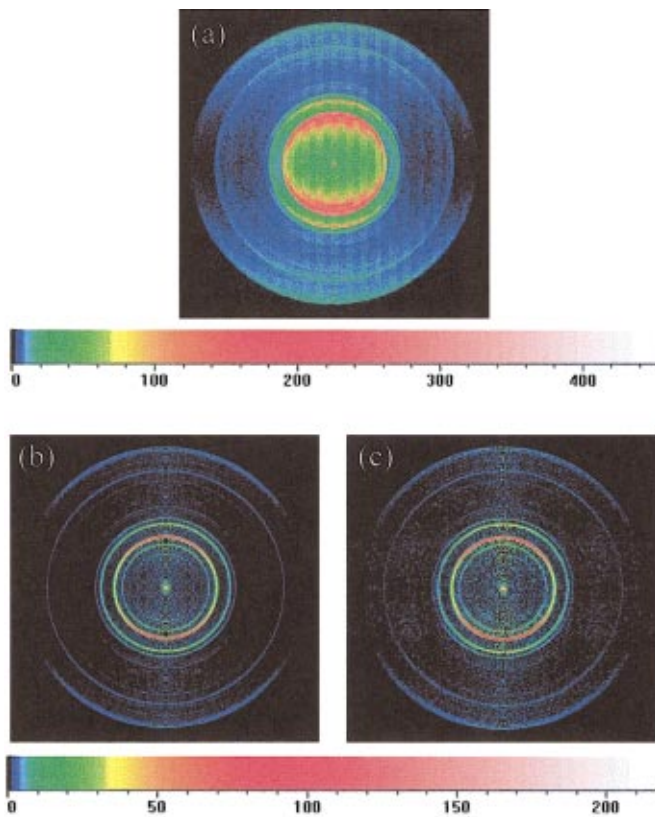


FIG. 8. (Color) (a) Experimental image (projection) obtained by monitoring O^+ from the dissociative photoionization of O_2 (multiphoton at 225.02 nm) using the single ion counting technique (Ref. 19). (b) 2D cut of the image reconstructed from the experimental projection using the BASEX method ($\sigma=2$), without prior smoothing of the data. (c) 2D cut of the image reconstructed using the Fourier-Hankel method (Ref. 1) after smoothing the experimental data by combining every four pixels of the image into one pixel.

tions without prior smoothing, and still exhibit very good resolution.

Shown in Fig. 8(b) is a 2D cut of the photoion image reconstructed from the projection in Fig. 8(a) by using the BASEX method without prior smoothing of the data. In order to obtain a reliable reconstruction of this image with the Fourier-Hankel method, it was necessary to decrease the point-to-point fluctuations by combining every four adjacent pixels into one pixel (thereby reducing the size of the image by a factor of 2 in each dimension).¹⁹ A 2D cut of the image reconstructed in this way is presented in Fig. 8(c). It is obvious that the reconstruction quality obtained by using the BASEX method is better. Figure 9 shows the corresponding speed distributions, which demonstrate that the BASEX method is capable of reconstructing weak features adjacent to intense ones (see the inset). These weak features are partially or totally obscured when using the Fourier-Hankel method because of the excessive reconstruction artifacts.

IV. DISCUSSION

A. Advantages of the BASEX method

The approach presented in this article features several advantages over the other methods commonly used for reconstruction of 3D, cylindrically symmetric images from their projections. First, for synthesized noise-free projec-

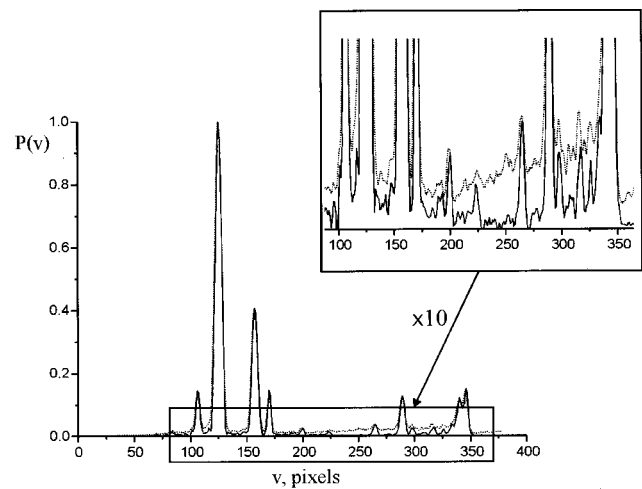


FIG. 9. Speed distributions obtained from the images shown in Fig. 8, reconstructed by using the BASEX (solid line) and the Fourier-Hankel (dotted line) method. The inset demonstrates the presence of low-intensity peaks (e.g., at pixels 95, 115, 190, and 220), which are revealed by the BASEX method, but are almost totally obscured by the noise generated in the Fourier-Hankel method.

tions, the BASEX method reconstructs an essentially exact and artifact-free image. This is in contrast to methods such as Fourier-Hankel, “onion peeling,” or iteration, which can converge to the exact solution only in the case of a continuous projection. In order to reconstruct the distribution from a discrete projection, these methods use interpolation procedures, thereby introducing additional errors or assumptions.

Second, the BASEX method is computationally cheap, as it requires only matrix multiplications, while the basis sets are generated and stored on a disk prior to image reconstruction. More precisely, for each basis set, the corresponding matrix needs to be calculated only once and stored in a separate file, which is called when reconstructing the experimental images. For example, on a computer with a Pentium II-300 MHz processor, reconstruction of the images with basis sets of 226×226 or 251×251 functions takes 1 to 2 min, with no effort to optimize the time performance.

Third, since the basis set used in the current work consists of functions that are localized and cover the space uniformly (see Sec. II B and Fig. 1), the reconstruction procedure does not accumulate noise in any specific region of the reconstructed image. Noise in the image appears only when it exists in the projection; it is not generated by the inversion procedure. However, it is important to realize that each point of the original 3D image, located at a distance r_0 from the axis of cylindrical symmetry, contributes only to points with $x \leq r_0$ in the projection [this can be easily seen from Eq. (1)]. Thus the projection contains less information about regions of the image closer to the symmetry axis compared to those farther from the axis. In particular, only the $x=0$ points in the projection contain information about the center-line ($r_0=0$) of the original image, while information about points with $r_0=r_{\max}$ is contained in every point of the projection. Since the noise is usually distributed evenly throughout the measured projection, the signal-to-noise ratio in the reconstructed image decreases towards the centerline. This is especially noticeable in images reconstructed with the Fourier-

Hankel method. Employing Tikhonov regularization in the BASEX method enables us to reduce significantly this centerline noise without affecting the reconstruction quality.

Fourth, the resolution in the reconstructed image is superior to that obtained with the Fourier–Hankel method, particularly for noisy projections. The reason is that the basis functions used are sufficiently narrow, and thus are capable of reproducing even the sharpest features obtained with current imaging technology. Note, however, that since the Gaussian basis set was specifically constructed for images that have a well-defined center, centering the image is crucial for obtaining maximum resolution; e.g., a deviation of even one pixel from the center causes a decrease in resolution. In fact, this feature can be used to find the exact center of the image.

Fifth, the image reconstructed using the BASEX method has an exact analytical expression and thus allows an analytical calculation of the speed distribution, which gives a better-resolved speed distribution than the one obtained from the discrete image in other methods. This is achieved without increasing the computation time.

B. Improvements and extensions

The reconstruction algorithm described in this article is flexible and allows modifications that can further improve its performance in specific applications. The Gaussian basis set used in the present work does not assume any special properties of the image, except the existence of cylindrical symmetry. It is thus most appropriate for general applications without requiring input from the user. However, for particular sets of problems, special types of basis sets containing functions with properties resembling those of the reconstructed images can be used without loss of fidelity. This can reduce the number of basis functions needed to describe the image and may improve the quality of the fit.

In addition, although Tikhonov regularization was found to provide considerable improvement in the quality of the reconstruction near the symmetry axis for all images processed, other regularization techniques²⁰ may be found to be more efficient in treating noisy signals in specific cases.

The method has been used successfully by the authors to analyze a wide variety of images, and the code and examples are available upon request.²¹

ACKNOWLEDGMENTS

The authors wish to thank D. H. Parker, A. Eppink, M. Janssen, and A. Sanov for sending projections and images, and for testing the method with their synthetic and experimental images and comparing the results with other methods. In particular the authors thank A. Eppink for providing the image shown in Fig. 8 and its reconstruction by the Fourier–Hankel method. A. Demyanenko and A. Potter have carried out extensive testing of the method, and we benefited greatly from their input. Support by the National Science Foundation, NSF Grant Nos. CHE-9900745 (HR) and CHE-0108823 (VAM), and by the Donors of the Petroleum Research Fund, administered by the American Chemical Society (to H.R.) is gratefully acknowledged. V.A.M. is an

A.P. Sloan Research Fellow. H.R. would like to thank the Departments of Chemistry and Physics at the University of California, Irvine, and in particular Professor Wilson Ho, for their hospitality during her sabbatical leave.

APPENDIX

In the numerical evaluation of $\rho_k(r)$ and $\chi_k(x)$, problems may be encountered when dealing simultaneously with extremely large and small numbers. In addition, the calculation of $\chi_k(x)$ can be time-consuming since, according to Eq. (15), the number of terms in the summation increases as k^2 . Below we describe a procedure to overcome these difficulties.

Let us define the function

$$R_n(u) = \left(\frac{e}{n}\right)^n u^{2n} e^{-u^2} \tag{A1}$$

$$= \exp\left[n - u^2 + n \ln\left(\frac{u^2}{n}\right)\right]. \tag{A2}$$

With this notation, $\rho_k(r) = R_{k^2}(r/\sigma)$. Expression (A2) can be used to evaluate $R_n(u)$ at any u . Note that the argument of the exponent is $n - u^2 + n \ln(u^2/n) \leq 0$ and is exactly zero at $u = \sqrt{n}$. Furthermore, to a very good approximation, $R_n(u) \approx e^{-2(u-\sqrt{n})^2}$, which can be seen by expanding the logarithm in a Taylor series around $u = \sqrt{n}$:

$$\begin{aligned} \ln\left(\frac{u^2}{n}\right) &= \ln\left(1 + \frac{u^2 - n}{n}\right) \approx \frac{u^2 - n}{n} - \frac{(u^2 - n)^2}{2n^2} = \frac{u^2 - n}{n} \\ &\quad - \frac{(u - \sqrt{n})^2(u + \sqrt{n})^2}{2n^2} \approx \frac{u^2 - n}{n} - \frac{2(u - \sqrt{n})^2}{n}. \end{aligned}$$

Therefore $R_n(u)$ is essentially zero outside some small interval around $u = \sqrt{n}$ and needs to be computed only inside this interval.

The Abel transform of $R_n(u)$ is given by

$$X_n(u) = 2\gamma_n \sum_{l=0}^n \frac{\alpha_l}{\gamma_{n-l}} R_{n-l}(u), \tag{A3}$$

with

$$\gamma_l = (e/l)! l!,$$

and

$$\alpha_l = \prod_{m=1}^l \left(1 - \frac{1}{2m}\right),$$

for $l > 0$ and $\alpha_0 = 1$.

Because the coefficients α_l and γ_l are of the order of one for any l , Eq. (A3) is suitable for numerical evaluation and can be used to compute $\chi_k(x) = X_{k^2}(x/\sigma)$. Furthermore, for any particular u only a few terms with $n - l \sim u^2$ contribute to the sum in Eq. (A3). This makes the calculation of $\chi_k(x)$ very fast.

¹A. G. Suits and R. E. Continetti, ACS Symp. Ser. **770** (2001) and papers therein.

²A. T. J. B. Eppink and D. H. Parker, Rev. Sci. Instrum. **68**, 3477 (1997).

- ³Y. Tanaka, M. Kawasaki, Y. Matsumi, H. Fujiwara, T. Ishiwata, L. J. Rogers, R. N. Dixon, and M. N. R. Ashfold, *J. Chem. Phys.* **109**, 1315 (1998).
- ⁴B.-Y. Chang, R. C. Hoetzlein, J. A. Mueller, J. D. Geiser, and P. L. Houston, *Rev. Sci. Instrum.* **69**, 1665 (1998).
- ⁵F. B. Hildebrand, *Methods of Applied Mathematics* (Prentice-Hall, Englewood Cliffs, NJ, 1952).
- ⁶R. N. Bracewell, *The Fourier Transform and its Applications* (McGraw-Hill, New York, 1978).
- ⁷K. Bockasten, *J. Opt. Soc. Am.* **51**, 943 (1961).
- ⁸M. P. Freeman and S. Katz, *J. Opt. Soc. Am.* **53**, 1172 (1963).
- ⁹C. J. Cremers and R. C. Birkebak, *Appl. Opt.* **5**, 1057 (1966).
- ¹⁰L. M. Smith, D. R. Keefer, and S. I. Sudharsanan, *J. Quant. Spectrosc. Radiat. Transf.* **39**, 367 (1988).
- ¹¹Y. Sato, Y. Matsumi, M. Kawasaki, K. Tsukiyama, and R. Bersohn, *J. Phys. Chem.* **99**, 16307 (1995).
- ¹²C. Bordas, F. Paulig, H. Helm, and D. L. Huestis, *Rev. Sci. Instrum.* **67**, 2257 (1996).
- ¹³J. Winterhalter, D. Maier, J. Honerkamp, V. Schyja, and H. Helm, *J. Chem. Phys.* **110**, 11187 (1999).
- ¹⁴M. J. J. Vrakking, *Rev. Sci. Instrum.* **72**, 4084 (2001).
- ¹⁵R. N. Strickland and D. W. Chandler, *Appl. Opt.* **30**, 1811 (1991).
- ¹⁶A. N. Tikhonov, *Sov. Math. Dokl.* **4**, 1035 (1963).
- ¹⁷R. N. Zare, *Angular Momentum: Understanding Spatial Aspects in Chemistry and Physics* (Wiley, New York, 1988).
- ¹⁸V. Dribinski, A. B. Potter, A. V. Demyanenko, and H. Reisler, *J. Chem. Phys.* **115**, 7474 (2001).
- ¹⁹D. H. Parker and A. T. J. B. Eppink, *J. Chem. Phys.* **107**, 2357 (1997); (private communication).
- ²⁰A. Neumaier, *SIAM Rev.* **40**, 636 (1998).
- ²¹A Windows-compatible version of the code is available by contacting H. Reisler at reisler@usc.edu